

---

AI translation · View original & related papers at  
[chinaxiv.org/items/chinaxiv-202306.00346](https://chinaxiv.org/items/chinaxiv-202306.00346)

---

## Postprint: Advances in X-ray Burst Oscillation Research

**Authors:** Li Qingxin, Li Zhaosheng

**Date:** 2023-06-07T00:00:00+00:00

### Abstract

X-ray burst oscillations are periodic phenomena detected in Type I X-ray bursts from low-mass X-ray binaries, with oscillation periods close to the neutron star's spin period. In recent years, high-energy detectors such as RXTE and NICER have detected burst oscillation phenomena in 30 low-mass X-ray binaries. X-ray burst oscillations hold significant importance for studying the state of dense matter, strong gravity on neutron star surfaces, and strong magnetic field behavior. This article introduces the search methods for Type I X-ray bursts and burst oscillations, observational results of burst oscillations, the hot spot model and surface mode oscillation model for burst oscillations; in the future, X-ray burst oscillations will be used to measure neutron star mass, radius, and spin.

### Full Text

### Preamble

ChinaXiv Cooperative Journal, Vol. 39, No. 2

### June 2021

**Progress in Astronomy** Vol. 39, No. 2, June 2021

doi: 10.3969/j.issn.1000-8349.2021.02.03

### Research Progress of X-ray Burst Oscillations

LI Qing-xin, LI Zhao-sheng

(School of Physics and Optoelectronic Engineering, Xiangtan University, Xiangtan 411105)

### Abstract

X-ray burst oscillations are periodic phenomena detected in Type I X-ray bursts from low-mass X-ray binaries (LMXBs), with oscillation periods close to the neu-

tron star spin period. In recent years, high-energy detectors such as RXTE and NICER have observed burst oscillations in 30 LMXB sources. X-ray burst oscillations are significant for studying the properties of dense matter, strong gravity, and strong magnetic fields on neutron star surfaces. This paper introduces Type I X-ray bursts and the search methods for burst oscillations, presents observational results of burst oscillations, and discusses theoretical models including the hot spot model and surface mode oscillation model. In the future, X-ray burst oscillations will be used to measure neutron star masses, radii, and spin rates.

**Keywords:** X-ray burst; X-ray burst oscillation; Low-mass X-ray binary; Pulsar

**Classification Code:** P142.6

**Document Code:** A

## 1 Introduction

Low-mass X-ray binaries (LMXBs) consist of a compact star (neutron star or black hole) and a low-mass main-sequence companion ( $M < M_{\odot}$ ). Their X-ray emission originates from accretion onto the compact object. When the compact object is a neutron star, accreted material accumulates on the stellar surface under conditions of extreme temperature, pressure, and strong gravitational fields, triggering unstable nuclear burning that manifests observationally as Type I X-ray bursts [?]. Strohmayer et al. [?] first detected X-ray burst oscillations (XBO) in LMXB 4U 1728-34 using the Rossi X-ray Timing Explorer (RXTE), leveraging its high time resolution and large effective area to identify a periodic signal at 363 Hz during a Type I X-ray burst. In 2003, Chakrabarty et al. [?] discovered periodic signals in Type I X-ray bursts from the accreting millisecond pulsar SAX J1808.4-3658, where the XBO frequency deviated from the spin frequency by only  $\sim 6 \times 10^{-3}$  Hz during the burst tail. In the same year, Strohmayer et al. [?] observed similar phenomena in another accreting millisecond pulsar, XTE J1814-338. These observations confirmed that XBO sources are nuclear-powered pulsars, with pulse radiation energy originating from nuclear burning on the stellar surface.

Based on observations from RXTE, Swift, and NICER, approximately 20% of Type I X-ray bursts in LMXB sources exhibit XBO phenomena, with oscillation frequencies ranging from  $\sim 11$  to 620 Hz and root-mean-square amplitudes between 5% and 20%, occasionally approaching 50% in some sources. In accreting millisecond pulsars, the observed XBO frequencies closely match the stellar spin frequencies, with differences within a few hertz. During the rise and decay phases of Type I X-ray bursts, the XBO frequency drifts by several hertz, typically asymptotically approaching the neutron star's spin frequency near the burst tail, where XBO signals are most readily detected.

Strohmayer et al. [?] proposed that XBO signals originate from neutron star rotation, suggesting that hot spots may form on the neutron star surface during

Type I X-ray bursts, creating an asymmetric temperature distribution that produces periodic signals in the X-ray band as the star rotates. However, questions regarding how these hot spots form and evolve during burst processes remain unresolved. Surface mode models (such as Rossby modes) propose that Type I X-ray bursts can excite oscillations in the neutron star ocean, creating temperature gradients at different heights on the stellar surface that, when modulated by rotation, produce XBO. These models can only partially explain observed XBO phenomena and require further refinement.

This paper separately introduces Type I X-ray bursts, XBO observations, and oscillation theories.

## 2 Type I X-ray Bursts

Type I X-ray bursts are unstable nuclear burning events in neutron star LMXBs, primarily involving hydrogen burning, helium burning, and carbon burning. Carbon burning manifests observationally as superbursts, first discovered by Grindlay et al. [?] in 4U 1820-30. Typical Type I X-ray burst light curves exhibit rapid rises followed by exponential decays, with rise times of  $\sim 1\text{--}10$  s (see Figure 1 [Figure 1: see original paper]), durations of 10–100 s, and recurrence intervals of hours to days. The energy spectra are generally fitted with blackbody models with characteristic temperatures of 1–3 keV, releasing total energies of  $10^{32}\text{--}10^{33}$  J. Type I X-ray bursts have been observed in 115 neutron star LMXB sources [?].

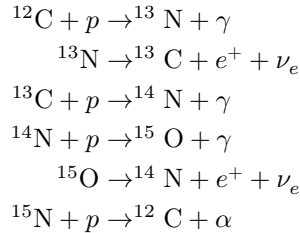
The nuclear burning processes in Type I X-ray bursts sensitively depend on the local accretion rate onto the neutron star. The local Eddington accretion rate is defined as:

$$\dot{m}_{\text{Edd}} = \frac{(1+X)R\sigma_T}{H} \approx 1.5 \times 10^5 \frac{g}{\text{cm}^2 \cdot \text{s}} \frac{1+X}{10 \text{ km}}$$

where  $m_p$  is the proton mass,  $c$  is the speed of light,  $X$  is the hydrogen abundance in the atmosphere,  $\sigma_T$  is the Thomson scattering cross-section, and  $R$  is the neutron star radius. For solar abundance ( $X = 0.73$ ) and a 10 km neutron star, the local Eddington accretion rate is  $8.8 \times 10^4 \text{ g cm}^{-2} \text{ s}^{-1}$ .

### 2.1 Hydrogen Burning

At relatively low neutron star surface temperatures, hydrogen burning is dominated by the cold CNO cycle, with the hot CNO cycle occurring in rare cases. At sufficiently high surface temperatures, hydrogen burning proceeds primarily through the rp-process. The cold CNO cycle proceeds as follows:



During the cycle, C, N, and O nuclei capture protons and release  $\alpha$ -particles in the final step, with production and consumption rates of C, N, and O being equal, making them catalysts for the process. The cold CNO reaction rate depends on proton capture rates, particularly the  $^{14}\text{N}(p, \gamma)^{15}\text{O}$  reaction. When the accretion rate is below  $0.01 \dot{m}_{\text{Edd}}$ , hydrogen burns through the cold CNO cycle with extremely rapid reaction rates. The energy release is proportional to  $T^{16}$  (where  $T$  is the environmental temperature), making the process unstable and triggering helium burning. Observationally, this manifests as mixed H/He burning Type I X-ray bursts.

## 2.2 Helium Burning

Helium-rich shells can form beneath stable hydrogen-burning layers (for accretion rates  $0.01 \dot{m}_{\text{Edd}} - 0.1 \dot{m}_{\text{Edd}}$ ) or through accretion from helium white dwarfs or helium-rich main-sequence companions. In helium shells, when the accretion rate is  $0.1 \dot{m}_{\text{Edd}} - 1 \dot{m}_{\text{Edd}}$ , environmental temperatures are high ( $T > 10^8$  K), and degenerate electron densities reach  $10^6$  g/cm<sup>3</sup>, unstable helium burning is triggered (reaction rate  $\propto T^{30}$ , making this process extremely unstable). The helium burning process is  $\alpha + \alpha + \alpha \rightarrow ^{12}\text{C} + \gamma$ . This occurs in two stages: first, two  $\alpha$ -particles combine to form  $^8\text{Be}$ , which has a lifetime of only  $2.6 \times 10^{-16}$  s; continuous formation of  $^8\text{Be}$  provides sufficient particles to combine with another  $\alpha$ -particle to form the excited state  $^{12}\text{C}^*$  (the second stage of the  $3\alpha$  process). The  $^{12}\text{C}^*$  can decay back to  $^8\text{Be}$  and release an  $\alpha$ -particle, or radiate a  $\gamma$ -photon to reach the carbon ground state. Observationally, this manifests as helium-burning Type I X-ray bursts, which have shorter rise and decay times compared to mixed H/He burning bursts.

## 2.3 Carbon Burning

In a few sources (e.g., 4U 1820-30), a special class of X-ray bursts called superbursts has been observed. Compared to the two types of Type I X-ray bursts described above, superbursts release about  $10^3$  times more total energy, last approximately  $10^3$  times longer, and occur much less frequently. These bursts likely originate from carbon burning in deeper layers of the neutron star atmosphere. Currently, the conditions for superburst occurrence remain unclear and

may require additional heating mechanisms (such as superdense nuclear reactions in the neutron star crust) to overcome the Coulomb barrier for carbon fusion.

### 3 Observations of X-ray Burst Oscillations

Detecting XBO requires high-energy X-ray telescopes with high time resolution, large effective area, and minimal photon pile-up and dead-time effects. Since RXTE first discovered XBO in neutron star LMXBs in 1996, this phenomenon has been found in 30 sources to date. The XBO frequencies are listed in Table 1, where sources with confirmed burst oscillation frequencies are categorized as pulsars or non-pulsars, while sources requiring further observational verification are listed separately. In addition to RXTE, XBO signals have been searched for in observations from Swift/BAT and NICER. Below, we describe the search methods for XBO signals, probability estimation for signals, and X-ray telescope observations of XBO.

#### 3.1 Methods for Searching XBO

Periodic XBO signals can be searched using Fast Fourier Transform (FFT) or  $Z_n^2$  statistics [?], which are designed for binned data and event data, respectively [?].

For FFT, the light curve with total duration  $T$  is uniformly divided into  $N$  bins, where  $N = 2^m$  (with  $m$  an integer). The time series is denoted as  $x_k$  ( $k = 0, 1, 2, 3, \dots, N - 1$ ), representing the photon count in the  $k$ -th bin. The Leahy-normalized power density spectrum  $P_j$  is given by [?]:

$$P_j = \frac{2}{N_{\text{tot}}} \left[ \left( \sum_{k=0}^{N-1} x_k \cos 2\pi\nu_j t_k \right)^2 + \left( \sum_{k=0}^{N-1} x_k \sin 2\pi\nu_j t_k \right)^2 \right]$$

where  $\nu_j$  is the Fourier frequency ( $\nu_j = j/T$ ,  $j = 0, 1, 2, 3, \dots, N/2$ ) and  $N_{\text{tot}}$  is the total photon count. The minimum frequency in the power density spectrum is  $\nu_{\text{min}} = 1/T$ , the maximum frequency (Nyquist frequency) is  $\nu_{\text{max}} = N/(2T)$ , and the frequency resolution is  $\Delta\nu = 1/T$  [?].

Event data records the arrival time of each photon and can be converted to binned data; binned data records the photon count rate in each time interval [?].

The  $Z_n^2$  method is similar to FFT for computing power density spectra and is defined as [?]:

$$Z_n^2 = \frac{2}{N_\gamma} \sum_{k=1}^n \left[ \left( \sum_{j=1}^{N_\gamma} \cos k\phi_j \right)^2 + \left( \sum_{j=1}^{N_\gamma} \sin k\phi_j \right)^2 \right]$$

where  $n$  is the number of harmonics and  $\phi_j$  is the photon phase:

$$\phi_j = 2\pi \int_{t_0}^{t_j} \nu(t) dt$$

where  $t_0$  is the reference time,  $t_j$  is the photon arrival time relative to  $t_0$ , and  $\nu(t)$  is the frequency model. When  $\nu(t)$  is constant,  $\phi_j = 2\pi\nu t_j$ .

In addition to oscillation frequency, the power spectrum contains information about pulse amplitude. For Leahy-normalized power spectra, the root-mean-square (rms) fractional amplitude is defined as:

$$A_{\text{rms}} = \sqrt{\frac{N_\gamma}{N_\gamma - B} \frac{P_s - P_n}{N_\gamma}}$$

where the bracketed term corrects for background effects,  $N_\gamma$  is the total photon count,  $B$  is the background photon count [?],  $P_s$  is the signal power, and  $P_n$  is the noise power. If using the  $Z_n^2$  method, replace  $P_s$  in equation (5) with  $Z_n^2$ .

Compared to FFT, the  $Z_n^2$  method can measure oscillation frequencies more accurately but requires longer computation time. Typically, for event data from Type I X-ray bursts, the data are first converted to binned format, then FFT is used to search for XBO signals. If a signal (or candidate signal) is detected,  $Z_n^2$  can be applied for more precise frequency measurement.

### 3.2 Estimating the Probability of a Genuine Signal

After finding candidate XBO signals using FFT or  $Z_n^2$  statistics, it is necessary to determine the probability that the signal is real and to derive the probability distribution of the true signal from the measured XBO signal.

**3.2.1 Estimating True Signal Probability for FFT** The power density spectrum of Type I X-ray bursts calculated by FFT contains red noise and Poisson noise at low frequencies, while high frequencies are dominated by Poisson noise. Power densities generated by Poisson noise follow a  $\chi^2$  distribution with two degrees of freedom [?]:

$$p(R_n, I_n) = \frac{1}{\pi} \exp[-(R_n^2 + I_n^2)]$$

where  $R_n$  and  $I_n$  are the real and imaginary parts of the noise Fourier transform coefficients. According to Groth's [?] analytical expression, the probability distribution of measured power  $P_m$  and signal power  $P_s$  is:

$$p_k(P_m, P_s) = \frac{1}{2} \left( \frac{P_m}{P_s} \right)^{(k-1)/2} \exp \left[ -\frac{1}{2}(P_m + P_s) \right] I_{k-1}(\sqrt{P_m P_s})$$

where  $I$  is the modified Bessel function of the first kind and  $k$  is the number of harmonics (generally taken as 1). For the noise-only case,  $P_s = 0$  and  $k = 1$ , equation (7) becomes the probability density function (pdf) of a  $\chi^2$  distribution with two degrees of freedom:  $p_1(P_m, 0) = \exp(-P_m/2)$ . For  $k > 1$ ,  $p_k(P_m, 0)$  follows a  $\chi^2$  distribution with  $2k$  degrees of freedom.

**3.2.2 Estimating True Signal Probability for  $Z_n^2$  Statistics** If  $Z_n^2$  statistics indicate that the probability of the signal being generated by noise is less than 1%, the signal is considered genuine. Following the method used by Ootes et al. [?] for processing RXTE burst data in 2017, the search range is defined as approximately  $\pm 5$  Hz around the measured oscillation frequency. As shown in Figure 2 [Figure 2: see original paper], the number of trials is defined as the total number of time-frequency windows:  $N = N_t \times N_\nu$ , where  $N_t$  is the number of time windows and  $N_\nu$  is the number of frequency windows.

Assuming Poisson-distributed noise, the probability  $P_{\text{noise}}$  that the measured signal originates from noise distribution  $\delta$  is:

$$P_{\text{noise}} = N\delta(1 - \delta)^{N-1}$$

Based on  $P_{\text{noise}} \leq 1\%$ , Muno et al. [?] defined three criteria for identifying significant signals: (1) Substituting  $N = N_t \times N_\nu = 16 \times 10 = 160$  trials and  $P_{\text{noise}} \leq 1\%$  into equation (9) yields noise distribution  $\delta \leq 7 \times 10^{-5}$ . (2) Calculating the first second of the burst rise phase ( $N_t = 1$ ) with  $P_{\text{noise}} \leq 1\%$  gives  $\delta \leq 10^{-3}$ . (3) For a time-frequency window with two adjacent frequency windows and one adjacent time window, the noise probability for the selected window and one adjacent window is given by the product of their independent noise probabilities:  $\text{Prob}_{1,2} = P_1(N_1, \delta_1) \times P_2(N_2, \delta_2)$ . Since three adjacent windows can be used, with one having  $N_\nu = 3$ , this can be approximated as:

$$\text{Prob}_{1,2} \approx 3N_t^2 N_\nu \delta_1 \delta_2$$

When  $\text{Prob}_{1,2} \leq 10^{-2}$ , substituting into equation (10) gives  $\delta_1 \delta_2 \leq 1.3 \times 10^{-6}$ .

These criteria and the fact that  $Z_n^2$  statistics follow a  $\chi^2$  distribution with  $2n$  degrees of freedom (typically  $n = 1$ ) can determine whether the power is from a genuine signal. For a given signal power  $Z_s$ , the conditional probability distribution  $p_k$  of measured signal  $Z_m$  satisfies [?]:

$$p_k(Z_m|Z_s) = \frac{1}{2} \left( \frac{Z_m}{Z_s} \right)^{(k-1)/2} \exp \left[ -\frac{1}{2}(Z_m + Z_s) \right] I_{k-1}(\sqrt{Z_m Z_s})$$

where  $k$  is the number of harmonics (generally  $k = 1$ ) and  $I_{k-1}$  is the modified Bessel function of the first kind. The probability of measuring power between

0 and  $Z_m$  given  $Z_s$  is obtained through the associated cumulative distribution function:

$$f_k(Z_m|Z_s) = 1 - \exp\left[-\frac{1}{2}(Z_m + Z_s)\right] \sum_{l=0}^{k+n-1} \frac{(Z_s)^n (Z_m)^l}{l!n!2^{n+l}}$$

The probability that the true signal power lies between 0 and  $Z_s$  given  $Z_m$  is:

$$f_k(Z_s|Z_m) = 1 - f_k(Z_m|Z_s)$$

If no oscillation signal is found throughout the burst, the maximum power is selected as the upper limit.

**3.2.3 Monte Carlo Simulations** Monte Carlo simulations can evaluate the distribution of noise power in the absence of signals and accurately model actual observational conditions such as specified time windows. First, an appropriate model is selected to fit the Type I X-ray burst light curve, then numerous light curve samples are generated with Poisson counting statistics but without any periodic signals. Power spectra obtained from these simulated light curves yield the power density distribution from noise alone. By statistically analyzing the power distribution near the measured oscillation signal, the noise distribution can be determined, allowing assessment of the probability that the measured XBO signal originates from noise.

### 3.3 Dynamic Power Density Spectrum of XBO

Strohmayer et al. [?] applied FFT to the entire Type I X-ray burst light curve and found multiple peaks in the power density spectrum (see Figure 1), indicating that the XBO frequency evolves with time during the burst. To effectively search for and track XBO signals, dynamic power density spectrum methods are generally used to analyze Type I X-ray bursts.

Figure 3 [Figure 3: see original paper] illustrates the process of generating dynamic power spectra. Figure 3a shows the Type I X-ray burst light curve, which can be divided into multiple segments (three segments are shown here).  $\Delta t_0$ ,  $\Delta t_1$ , and  $\Delta t_2$  represent the time lengths of sliding windows, with overlap between adjacent windows, where  $T_0$ ,  $T_1$ , and  $T_2$  are the midpoints of the windows. Figure 3b shows the power density spectra calculated for each light curve segment, with blue representing low power, purple medium power, and red high power. Figure 3c combines the power density spectra from Figure 3b with their corresponding midpoints to produce a time-power-frequency three-dimensional diagram. Finally, Figure 3d projects the power contours from Figure 3c onto the light curve, yielding the dynamic power density spectrum, which concisely displays information about when XBO appears and how its frequency and intensity evolve with time.

### 3.4 RXTE Observations of XBO

The RXTE satellite was launched on December 30, 1995, and officially decommissioned on January 5, 2012, after 16 years of operation. It remains the most important and successful high-energy timing detector for XBO research to date. RXTE recorded high time resolution data in event mode. In 2019, Bilous and Watts [?] systematically searched for XBO signals in all RXTE-observed Type I X-ray bursts using FFT, examining 2,118 bursts from 57 neutron star LMXB sources. They listed the signal-to-noise ratios at burst peaks, extracted light curves in the 2–60 keV energy range, used 2 s search windows with 0.5 s steps, provided information on burst oscillation frequencies and their occurrence phases, and calculated fractional amplitudes. For sources with previously determined oscillation frequencies, they confirmed that 17 known XBO frequencies matched previously measured frequencies or pulsar spin frequencies. They also re-examined sources with previously reported but unconfirmed burst oscillations, finding that some showed no oscillation signals while others had signals too weak to exclude noise (see Table 1 for details on sources with unconfirmed XBO frequencies). They also discovered a 531 Hz XBO signal from SAX J1810.8-2609 and an  $\sim 600$  Hz oscillation signal from IGR J17473-2721, with frequency variations within 3 Hz across different bursts from the latter source, suggesting it may be a new XBO source requiring further verification.

Galloway et al. [?] primarily used the  $Z_n^2$  method to search 7,083 bursts from 85 neutron star LMXB sources, extracting light curves in the 3–25 keV energy range and detecting 244 burst oscillations in 16 distinct sources. They provided probabilities for the authenticity of burst oscillation signals, information on frequency evolution with time, and the burst phases where the strongest signals were detected.

Figure 4 [Figure 4: see original paper] shows typical XBO dynamic power density spectra observed by RXTE. Figures 4a (SAX J1808.4-3658) and 4b (XTE J1814-338) are persistent accretion-powered pulsars; Figures 4c (HETE J1900.1-2455) and 4d (Aql X-1) are intermittent accretion-powered pulsars; and Figures 4e (4U 1636-536) and 4f (4U 1728-34) are non-pulsars.

Studies show that SAX J1808.4-3658 exhibits oscillation signals from the beginning of bursts, drifting up or down by several hertz as the burst progresses, suddenly disappearing at the burst peak, then reappearing at slightly higher or lower frequencies and stabilizing. XTE J1814-338 shows frequency variations within one Fourier frequency resolution, with oscillation signals not disappearing during the burst peak and often appearing in the burst tail. Persistent accretion-powered pulsars have oscillation frequencies very close to their spin frequencies, within a few hertz. HETE J1900.1-2455 shows only one time window with detected burst oscillation peaks, while lower-frequency oscillation signals persist for some time. Intermittent accretion-powered pulsars like Aql X-1 and HETE J1900.1-2455 show slowly drifting burst oscillation frequencies throughout the burst, asymptotically approaching maximum frequencies about 1 Hz lower than

the spin frequency. Non-pulsars like 4U 1636-536 show burst oscillation signals during the burst rise phase, while 4U 1728-34 shows signals throughout the entire burst. For non-pulsars, the observed burst oscillation frequencies drift upward by  $\sim 1$  Hz as the burst progresses, similar to intermittent accretion-powered pulsars, asymptotically approaching maximum frequencies near the burst tail.

RXTE also detected XBO phenomena from superbursts in neutron star LMXBs. Figure 5 shows the superburst light curve and dynamic power spectrum of 4U 1636-53 observed in 2001 by Strohmayer and Markwardt [?], clearly showing frequency drift in the dynamic power spectrum due to Doppler motion of the neutron star in its binary orbit. The superburst oscillation frequency is about 0.4 Hz higher than that of normal Type I X-ray bursts, making it closer to the neutron star's true spin frequency. Additionally, superburst oscillation signals were discovered in LMXB 4U 0614+09 [?].

### 3.5 NICER Observations of XBO

On June 3, 2017, NASA launched the Neutron star Interior Composition Explorer (NICER), designed to study neutron star composition and internal structure by precisely measuring neutron star masses and radii. NICER provides 56 co-aligned X-ray concentrator arrays, each equipped with a silicon drift detector operating in the 0.2–12 keV band with energy resolution of  $\sim 85$  eV at 1 keV and effective area exceeding  $2,000 \text{ cm}^2$  at 1.5 keV. Its time resolution is better than 300 ns, significantly superior to RXTE. NICER has become the primary and most capable instrument for XBO research following RXTE.

**3.5.1 SAX J1808.4-3658** Bult et al. [?] observed SAX J1808.4-3658 with NICER in 2019, detecting the expected 401 Hz XBO without significant frequency drift. They presented both the XBO pulse profile and the persistent emission pulse profile (Figure 6 [Figure 6: see original paper]), showing that the XBO profile and amplitude are similar to the persistent accretion pulse, indicating both originate from burning in a confined region on the neutron star surface (hot spot, see Section 5.1). However, the XBO leads the persistent pulse by  $34^\circ \pm 7^\circ$ , and the XBO waveform shows different energy dependence compared to persistent accretion pulsars, with burst oscillation signals generally detected at lower energies.

**3.5.2 4U 1728-34** From its commissioning through February 2019, NICER detected seven Type I X-ray bursts from 4U 1728-34. Mahmoodifar et al. [?] found XBO phenomena in three of these bursts, all appearing in the burst decay tails (Figure 7 [Figure 7: see original paper]) with very similar frequencies, consistent with previous observations.

Comparing these three tail oscillations reveals that bursts can be stronger in higher energy bands and may have different amplitudes and characteristics. Two oscillations were detected only in the high-energy band ( $E > 6$  keV) with very large fractional rms amplitudes of  $(48 \pm 9)\%$  and  $(46 \pm 9)\%$ . Both the hot spot

model (Section 5.1) and surface mode oscillation model (Section 5.2) struggle to explain such large-amplitude oscillations appearing in burst decay tails. If all locations on the neutron star surface heat and cool uniformly, insufficient temperature gradients can be produced on the surface. The cooling wake model [?] (see Section 5.3) suggests that high surface temperature gradients require earlier-burned regions to cool before later-burned regions. When burning reaches the equator, the flame spreads rapidly around it, increasing the temperature gradient across the entire neutron star surface, so significant temperature gradients exist primarily near the equatorial region [?].

#### 4 Relationship Between Accreting Millisecond X-ray Pulsars and XBO

Accreting millisecond X-ray pulsars (AMXPs) are rapidly rotating neutron stars powered by accretion (converting gravitational potential energy to X-ray radiation through accreted material from companion stars). The detection of XBO in AMXPs confirmed that XBO signals originate from neutron star rotation. Studying XBO in AMXPs provides better understanding of the physical mechanisms behind burst oscillations. These sources have independently measurable spin frequencies and are the only class where the effects of stellar magnetic fields and non-uniform fuel distribution can be studied.

AMXP XBO frequencies are very close to their spin frequencies, typically within a few hertz, though the offset varies among different AMXPs. For example, XTE J1814-338 shows XBO frequencies extremely close to the spin frequency, while SAX J1808.4-3658 and IGR J17511-3057 show burst oscillations that increase rapidly during the burst rise, slightly exceed the spin frequency, then stabilize within  $\sim 10$  mHz of the spin frequency in the burst tail [?, ?]. XBO phenomena also differ between AMXPs and non-pulsars. In non-pulsar Type I X-ray bursts, XBO appears only when the source is in a soft state (high accretion rate) [?], whereas XBO can be detected in AMXPs even in hard states (low accretion rates). Burst oscillation durations also differ: for SAX J1808.4-3658 and XTE J1814-338, oscillations persist throughout the entire burst, while for non-pulsars, although sometimes detected throughout the burst, most oscillations appear in the burst tail [?], similar to intermittent accretion-powered pulsars. IGR J17511-3057 represents a transition between these two behaviors: at low accretion rates, oscillations are detected throughout the burst, but as accretion rate increases, the oscillation signal disappears from the burst rise phase [?]. AMXPs also show higher harmonic content in their XBO signals compared to intermittent and non-pulsars [?, ?, ?], and their amplitude-energy relationships differ: AMXP XBO amplitudes decrease with increasing energy, while intermittent and non-pulsar XBO amplitudes increase with energy [?, ?]. XBO amplitudes vary significantly between sources, typically ranging from 1% to 10% of the persistent accretion-powered pulse amplitude during bursts [?, ?]. However, the transitional AMXP/radio pulsar IGR J18245-2452 is an exception: for one detected burst, the burst oscillation amplitude was much higher than

the accretion-powered pulse amplitude [?]. The reasons for these characteristic differences between pulsars and non-pulsars remain unclear, though dynamic magnetic fields may play a major role.

## 5 Theoretical Explanations of XBO

Observations show that in most bursts, oscillation frequencies drift upward (increase in frequency), generally appearing in burst tails, with some bursts showing very high amplitudes. In accreting pulsars, oscillation frequencies deviate from the spin frequency by only a few hertz. Studying ignition and flame propagation during bursts is crucial for understanding the physical mechanisms of burst oscillations. Current theoretical models include the hot spot model, surface mode oscillation model (Figure 8 [Figure 8: see original paper]), and cooling wake model. Cavecchi and Spitkovsky [?] simulated 3D models of unstable flame fronts during bursts in 2020, showing that unstable flame fronts accelerate overall burning and produce significant flame vortices, which are related to frequency drift and may excite surface oscillation modes.

### 5.1 Hot Spot Model

To explain the upward frequency drift and predominance of oscillations in burst tails, two hot spot models have been proposed: spreading hot spots that temporarily form during the burst rise phase as flames spread from ignition points across the neutron star, and confined burning restricted to small regions on the neutron star surface where hot spots persist.

Strohmayer et al. [?] first suggested that horizontal motion of flames spreading across the neutron star could cause frequency drift. To explain why frequencies consistently increase, they proposed that angular momentum conservation during vertical expansion of the burning layer causes rapid expansion to slow hot spot rotation, making observed frequencies lower than the spin rate. As the layer cools and contracts, frequencies increase, gradually approaching the spin frequency. In most burst tails, blackbody radii fitted to burst spectra are similar to neutron star radii, suggesting flames have burned across the entire surface [?]. However, accumulating burst fuel requires hours to days, while thermonuclear runaway occurs in less than 1 s [?]. To satisfy ignition conditions across the entire surface, thermal conditions must be uniform [?], but accretion asymmetries (such as magnetic channeling or equatorial boundary layers) make this unlikely, especially in AMXPs. Therefore, if burning begins at a point, flames must spread across the surface, but it remains difficult to explain how burning material can achieve the required thermal equilibrium.

The spreading hot spot model predicts that as the blackbody radius increases across the burst, hot spot size increases and oscillation amplitude decreases [?, ?, ?, ?]. This can explain burst oscillations during the rise phase but cannot account for most oscillations appearing in burst tails. One explanation is observational: the burst rise phase is very short, making detection difficult [?].

Another factor affecting XBO detectability is ignition latitude. On rapidly rotating neutron stars, effective gravity is lower at the equator where accretion rates are highest, making it easier to accumulate material for ignition [?]. Studies show that Type I X-ray bursts at the equator are more likely to exhibit detectable burst oscillations [?]. However, near the boundary layer, nuclear reaction processes in accreted material are intermediate between stable and unstable burning, potentially igniting at high latitudes [?]. In highly magnetized sources, magnetic poles may ignite preferentially due to locally high densities or excessive heating [?]. Flame propagation is also important for XBO detectability because flames must sustain propagation in asymmetric directions. The processes controlling flame spreading in Type I X-ray bursts have long been unresolved, influenced by heat conduction, turbulence, convection, and other transport mechanisms [?]. Spitkovsky et al. [?] highlighted the importance of hydrodynamic effects, particularly the interaction between Coriolis forces and expanding hot burning material. Coriolis forces slow flame propagation, preserving hot spots—crucial for controlling flame spread because rapid expansion and lateral diffusion could cause flame stall [?]. However, Coriolis force constraints are ineffective for IGR J17480-2446, which has a spin frequency of only 11 Hz [?].

High-amplitude oscillations in burst tails also lack definitive explanation. One mechanism is hot spot preservation where burning flames do not spread across the entire neutron star. One method to preserve hot spots is through magnetic field confinement of fuel. Accreted material flows along magnetic field lines to magnetic poles; when pressure is sufficient, field lines deform, allowing material to cross them. Brown and Bildsten [?] showed that magnetic field strengths of at least  $10^6$  T are required to confine material at typical Type I X-ray burst ignition depths—far higher than LMXB magnetic field strengths [?, ?]. Magnetohydrodynamic instabilities may also invalidate magnetic confinement [?], making this mechanism unlikely. Another mechanism involves confining the flame front: after burning begins and spreads some distance, propagation stops, requiring heat transport to be blocked in some manner. Cavecchi et al. [?] suggested that interaction between burning material and the radial magnetic field component could amplify the horizontal field component sufficiently to block heat conduction. For low-magnetic-field LMXBs, these processes are difficult to achieve unless some mechanism (such as convective dynamo action) temporarily increases the magnetic field during bursts [?].

## 5.2 Surface Mode Oscillation Model

The surface mode oscillation model proposes that ignition of Type I X-ray bursts and flame propagation around the neutron star may excite large-scale waves in the neutron star ocean (a plasma of ions and electrons extending from the outer layers to the depth where plasma crystallizes into a solid). Temperature differences at various heights in the ocean cause variations in X-ray brightness that, when modulated by stellar rotation, appear as XBO. Drawing from Earth

ocean surface mode studies, researchers have written fluid dynamics continuity equations (mass conservation), momentum and energy conservation equations for rotating spheres, simplified to Laplace's tidal equations [?, ?, ?]. The restoring forces for this system are buoyancy and Coriolis force. Non-axisymmetric mode solutions to Laplace's tidal equations depend on  $\exp(im\phi)$  in azimuthal angle  $\phi$ , where the azimuthal eigenvalue  $m$  is an integer. For a given neutron star rotation mode with azimuthal number  $m$  and frequency  $\nu_r$ , the observed frequency is:

$$\nu_o = m\nu_s + \nu_r$$

where  $\nu_s$  is the neutron star spin frequency and the sign of  $\nu_r$  depends on whether the mode propagates in the direction of rotation (eastward) or against it (westward). If  $\nu_r$  depends on the ocean's thermal state, it can explain XBO frequency drift, as oscillation frequencies would change as the burst progresses and the tail cools.

Laplace's tidal equations have three mode types: (1) Poincaré modes propagate westward and become pure gravity waves (restored solely by buoyancy) in the non-rotating limit, thus often called g-modes [?, ?]. (2) Kelvin modes propagate eastward (same direction as rotation) and become pure gravity waves in the non-rotating limit, but unlike Poincaré modes, Kelvin modes are in geostrophic balance (horizontal pressure gradient balanced by Coriolis force), involving only azimuthal motion and confined to equatorial flame propagation. (3) Rossby modes propagate westward, also called r-modes [?], driven by latitudinal variations in Coriolis force in the zero-buoyancy limit, becoming zero-frequency solutions in the non-rotating limit. With buoyancy from different burning materials, buoyancy also acts as a restoring force, hence they are often called buoyant r-modes.

Heyl [?] argued that buoyant r-modes are most likely: for example, retrograde-propagating modes with  $|\nu_r|$  of only a few hertz produce observed frequencies slightly below the spin frequency; as the burning layer cools,  $|\nu_r|$  decreases, and observed frequencies approach the spin frequency. Poincaré modes (or g-modes) predict much larger  $|\nu_r|$  and are thus excluded [?, ?]. Kelvin modes are excluded because their frequencies would decrease as the ocean cools, opposite to most observed frequency drifts. Kelvin and Poincaré modes also confine burning strictly to equatorial regions on rapidly rotating neutron stars, reducing overall burst oscillation amplitudes. Buoyant r-modes predict frequency drifts of  $\sim 10$  Hz during burning layer cooling, an order of magnitude higher than observed values. Piro and Bildsten [?] proposed that oscillations occur in the region between the burning layer base and neutron star crust, with frequency drifts of  $\sim 4$  Hz, still higher than measured values for AMXP sources. Heyl [?] noted that if buoyant r-modes are confined to the photosphere, drift frequencies could be smaller, though details require further study.

Some bursts temporarily exceed Eddington luminosity, converting thermal energy to kinetic and gravitational potential energy and causing expansion of the neutron star's outermost layers, known as photospheric radius expansion (PRE). Burst oscillations are typically detected from PRE bursts but rarely during the PRE phase itself. To explain the absence of oscillations during the peak phase, Cooper [?] considered efficient convective energy transport in the burning layer, analyzing single-zone models and finding that convection indeed suppresses oscillations, potentially explaining some tail-phase oscillations.

Chambers and Watts [?] considered frame-dragging and gravitational redshift effects in buoyant r-modes, calculating frequency drifts of  $\sim 1\text{--}3$  Hz that match observations but still predicting larger deviations between oscillation frequencies and spin frequencies than observed.

### 5.3 Cooling Wake Model

Large-amplitude burst oscillation signals detected in some X-ray burst tails cannot be explained by conventional hot spot models due to the lack of strong temperature gradients. Cumming and Bildsten [?] proposed that temperature gradients formed by cooling of the neutron star surface could cause tail-phase oscillations—the cooling wake model.

Mahmoodifar and Strohmayer [?] proposed three cooling wake models. Two “canonical” cooling wake models assume: (1) each region on the neutron star burns and cools identically—once ignition occurs at a point and flames spread to each region, the region temperature rises and falls exponentially, creating temperature gradients across the surface that, combined with neutron star spin, produce burst oscillation signals in the tail; (2) a latitude-dependent model where cooling times vary with latitude (the “canonical” model). On rapidly rotating neutron stars, effective gravitational acceleration decreases toward the equator and is maximum at the poles, so mass accretion rates and cooling times are maximum at the equator and minimum at the poles. Although this model incorporates cooling time variations, it maintains spin-axis symmetry. The third model is an asymmetric cooling phenomenological model where cooling time variations no longer satisfy spin-axis symmetry and individual region temperature variations are not considered—only temperatures of burned (hot) and unburned (cool) regions are considered. When flames spread across the entire neutron star surface, the timescale is short ( $\sim 1$  s) and surface temperature gradients are negligible. When cooling begins, earlier-burned regions cool first. Assuming cooling spreads like burning but over longer timescales ( $\sim 10$  s), earlier-burned regions not only cool first but also cool much faster than other regions, increasing burst tail oscillation amplitudes.

## 6 Applications

### 6.1 Measuring Neutron Star Mass and Radius

Precise measurement of neutron star mass and radius is crucial for understanding the dense matter equation of state and neutron star internal structure. Neutron star masses and radii in LMXBs can be determined through several independent methods: time-resolved spectroscopy of photospheric radius expansion bursts [?], fitting quiescent thermal spectra with known distances [?], and measuring mass-to-radius ratios from surface spectral features [?]. Pulse profile fitting can also measure neutron star mass and radius. X-ray pulsars exhibit pulsed radiation due to periodic rotation of surface hot spots. Under strong gravitational fields, hot spot radiation beams are bent, so observed pulse profiles depend on the neutron star's mass-to-radius ratio, as well as hot spot shape and viewing angle. Psaltis et al. [?] studied rapidly rotating accreting X-ray pulsars (spin frequencies 180–620 Hz) where high-speed rotation deforms the star, significantly altering pulse profiles. This effect, independent of light bending, provides additional mass-radius constraints, enabling mass and radius measurements without distance measurements. NICER's primary scientific goal is studying the composition of rotation-powered X-ray pulsars (where radiation energy comes from spin-down). NICER has accumulated extensive observational data, measuring the mass and radius of PSR J0030+0451 [?] and constraining dense matter states. This method depends on radiation photons originating from the neutron star surface rather than the magnetosphere. Pulse profile fitting methods applied to X-ray pulsars are also applicable to XBO. High-precision mass and radius measurements require detecting  $10^6$  photons. The future China-led eXTP mission will carry large-area detectors, measuring XBO from neutron star LMXBs, accumulating pulse profiles from multiple observations, and providing stricter constraints on neutron star composition. With 30 neutron star LMXBs (accretion-powered) already showing XBO, the observational sample far exceeds that of rotation-powered X-ray pulsars, enabling more neutron star mass and radius measurements across a wider mass spectrum [?]. Combined with masses and radii measured by other methods, this will effectively reduce measurement uncertainties.

### 6.2 Measuring Neutron Star Spin

For decades, multi-wavelength observations have been used to search for and study neutron stars, investigating their spin frequency distribution and evolution as important factors for understanding stellar and binary system evolution. Observations show that XBO frequencies in neutron star LMXBs are close to stellar spin frequencies, with errors of only a few hertz. XBO observations have independently discovered spin frequencies for many accretion-powered neutron stars. Observations of XBO from neutron star LMXB 4U 1608-522 revealed a spin frequency of  $\sim 620$  Hz, the fastest neutron star rotation measured in the X-ray band. Discovering more rapidly rotating neutron stars is crucial for understanding the recycling mechanism of radio millisecond pulsars, particularly mass

transfer, magnetic field decay, and accretion spin-up during accretion evolution. Another important question is the maximum spin frequency neutron stars can achieve. Sub-millisecond neutron stars would provide clean, strict constraints on the dense matter equation of state [?, ?, ?]. Whether burst oscillations can be observed on such rapidly rotating neutron stars remains an open question.

## 7 Conclusions and Outlook

This paper introduces XBO phenomena in neutron star LMXBs. Multiple theoretical models have been proposed to explain XBO observations, but these models struggle to explain all observed phenomena and require refinement. Currently, NICER has detected XBO and will observe more Type I X-ray bursts. The future China-led eXTP mission will also target neutron star observations as a primary research goal. We anticipate that XBO observations will discover sub-millisecond pulsars, precisely measure neutron star masses and radii, strictly constrain dense matter states, and establish more complete XBO theoretical models [?]. For example, we may discover massive ( $> 2M_{\odot}$ ) or low-mass ( $< 1M_{\odot}$ ) neutron stars. Accurate radius measurements of low-mass neutron stars would effectively distinguish between strange quark star and neutron star models. The existence of sub-millisecond neutron stars remains an open question.

## References

- [1] Strohmayer T E, Zhang W, Swank J H, et al. *ApJ*, 1996, 469: L9
- [2] Chakrabarty D, Morgan E H, Munro M P, et al. *Nature*, 2003, 424(6944): 42
- [3] Strohmayer T E, Markwardt C B, Swank J H, et al. *ApJ*, 2003, 596(1): L67
- [4] Grindlay J, Gursky H, Schnopper H, et al. *ApJ*, 1976, 205: L127
- [5] Bucccheri R, Bennett K, Bignami G F, et al. *A&A*, 1983, 128: 245
- [6] Leahy D A, Darbro W, Elsner R F, et al. *ApJ*, 1983, 266: 160
- [7] Bilous A V, Watts A L. *ApJS*, 2019, 245(1): 19
- [8] Groth E J. *ApJS*, 1975, 29: 285
- [9] Watts A L. *ARA&A*, 2012, 50: 609
- [10] Patruno A, Watts A L. *arXiv e-prints*, 2012: 143
- [11] Galloway D K, in't Zand J J M, Chenevez J, et al. *arXiv e-prints*, 2020: 32
- [12] Bult P, Jaisawal G K, Güver T, et al. *ApJ*, 2019, 885(1): L1
- [13] Linares M, Altamirano D, Watts A, et al. *The Astronomer's Telegram*, 2011, 3568: 1
- [14] Chakraborty M, Bhattacharyya S. *MNRAS*, 2012, 422(3): 2351
- [15] Altamirano D, Watts A, Linares M, et al. *MNRAS*, 2010, 409(3): 1136
- [16] Zhang W, Jahoda K, Kelley R L, et al. *ApJ*, 1998, 495(1): L9
- [17] Watts A L, Altamirano D, Linares M, et al. *ApJ*, 2009, 698(2): L174
- [18] Patruno A. *The Astronomer's Telegram*, 2013, 5068: 1
- [19] Galloway D K, Munro M P, Hartman J M, et al. *ApJS*, 2008, 179(2): 360
- [20] Kaaret P, in't Zand J J M, Heise J, et al. *ApJ*, 2002, 575(2): 1018
- [21] Strohmayer T E, Jahoda K, Giles A B, et al. *ApJ*, 1997, 486(1): 355

- [22] Strohmayer T E, Zhang W, Swank J H, et al. *ApJ*, 1998, 498(2): L135
- [23] Strohmayer T E, Markwardt C B. *ApJ*, 2002, 577(1): 337
- [24] Wijnands R, Strohmayer T, Franco L M. *ApJ*, 2001, 549(1): L71
- [25] Smith D A, Morgan E H, Bradt H. *ApJ*, 1997, 479(2): L137
- [26] Munro M P, Fox D W, Morgan E H, et al. *ApJ*, 2000, 542(2): 1016
- [27] Mahmoodifar S, Strohmayer T E, Bult P, et al. *ApJ*, 2019, 878(2): 145
- [28] Markwardt C B, Strohmayer T E, Swank J H. *ApJ*, 1999, 512(2): L125
- [29] Altamirano D, Linares M, Patruno A, et al. *MNRAS*, 2010, 401(1): 223
- [30] Bilous A V, Watts A L, Galloway D K, et al. *ApJ*, 2018, 862(1): L4
- [31] Villarreal A R, Strohmayer T E. *ApJ*, 2004, 614(2): L121
- [32] Galloway D K, Lin J, Chakrabarty D, et al. *ApJ*, 2010, 711(2): L148
- [33] Cavecchi Y, Patruno A, Haskell B, et al. *ApJ*, 2011, 740(1): L8
- [34] Kaaret P, Prieskorn Z, in 't Zand J J M, et al. *ApJ*, 2007, 657(2): L97
- [35] Thompson T W J, Rothschild R E, Tomsick J A, et al. *ApJ*, 2005, 634(2): 1261
- [36] Bhattacharyya S, Strohmayer T E, Markwardt C B, et al. *ApJ*, 2006, 639(1): L31
- [37] Kaaret P, in't Zand J J M, Heise J, et al. *ApJ*, 2003, 598(1): 481
- [38] Strohmayer T E, Markwardt C B, Kuulkers E. *ApJ*, 2008, 672(1): L37
- [39] Fox D W, Lewin W H G, Rutledge R E, et al. *MNRAS*, 2001, 321(4): 776
- [40] Galloway D K, Chakrabarty D, Munro M P, et al. *ApJ*, 2001, 549(1): L85
- [41] Bhattacharyya S. *MNRAS*, 2007, 377(1): 198
- [42] Altamirano D, Casella P, Patruno A, et al. *ApJ*, 2008, 674(1): L45
- [43] Ootes L S, Watts A L, Galloway D K, et al. *ApJ*, 2017, 834(1): 21
- [44] Munro M P, Galloway D K, Chakrabarty D. *ApJ*, 2004, 608(2): 930
- [45] Chambers F R N, Watts A L, Keek L, et al. *ApJ*, 2019, 871(1): 61
- [46] Munro M P, Chakrabarty D, Galloway D K, et al. *ApJ*, 2002, 580(2): 1048
- [47] Munro M P, Özel F, Chakrabarty D. *ApJ*, 2003, 595(2): 1066
- [48] Watts A L, Altamirano D, Markwardt C B, et al. *The Astronomer's Telegram*, 2009, 2199: 1
- [49] Papitto A, Ferrigno C, Bozzo E, et al. *Nature*, 2013, 501: 517
- [50] Cavecchi Y, Spitkovsky A. *ApJ*, 2019, 882(2): 142
- [51] Strohmayer T E, Zhang W, Swank J H. *ApJ*, 1997, 487(1): L77
- [52] Shara M M. *ApJ*, 1982, 261: 649
- [53] Cumming A, Bildsten L. *ApJ*, 2000, 544(1): 453
- [54] Bhattacharyya S, Strohmayer T E. *ApJ*, 2006, 642(2): L161
- [55] Spitkovsky A, Levin Y, Ushomirsky G. *ApJ*, 2002, 566(2): 1018
- [56] Maurer I, Watts A L. *MNRAS*, 2008, 383(1): 387
- [57] Cooper R L, Narayan R. *ApJ*, 2007, 657(1): L29
- [58] Watts A L, Patruno A, van der Klis M. *ApJ*, 2008, 688(1): L37
- [59] Zingales M, Timmes F X, Fryxell B, et al. *ApJS*, 2001, 133(1): 195
- [60] Brown E F, Bildsten L. *ApJ*, 1998, 496(2): 915
- [61] Hartman J M, Patruno A, Chakrabarty D, et al. *ApJ*, 2008, 675(2): 1468
- [62] Hartman J M, Patruno A, Chakrabarty D, et al. *ApJ*, 2009, 702(2): 1673
- [63] Litwin C, Brown E F, Rosner R. *ApJ*, 2001, 553(2): 788
- [64] Boutloukos S, Miller M C, Lamb F K. *ApJ*, 2010, 720(1): L15

- [65] Longuet-Higgins M S. Philosophical Transactions of the Royal Society of London Series A, 1968, 262(1132): 511
- [66] Lou Y Q. ApJ, 2000, 540(2): 1102
- [67] Townsend R H D. MNRAS, 2005, 364(2): 573
- [68] Bildsten L, Ushomirsky G, Cutler C. ApJ, 1996, 460: 827
- [69] Heyl J S. ApJ, 2004, 600(2): 939
- [70] Papaloizou J, Pringle J E. MNRAS, 1978, 182: 423
- [71] Piro A L, Bildsten L. ApJ, 2005, 619(2): 1054
- [72] Cooper R L. ApJ, 2008, 684(1): 525
- [73] Chambers F R N, Watts A L. MNRAS, 2020, 491(4): 6032
- [74] Mahmoodifar S, Strohmayer T. ApJ, 2016, 818(1): 93
- [75] Li Z, Qu Z, Chen L, et al. ApJ, 2015, 798(1): 56
- [76] Li Z, Falanga M, Chen L, et al. ApJ, 2017, 845(1): 8
- [77] Li Z, Suleimanov V F, Poutanen J, et al. ApJ, 2018, 866(1): 53
- [78] Psaltis D, Özel F, Chakrabarty D. ApJ, 2014, 787(2): 136
- [79] Riley T E, Watts A L, Bogdanov S, et al. ApJ, 2019, 887(1): L21
- [80] Lattimer J M, Prakash M. Phys Rep, 2007, 442(1-6): 109
- [81] Schaffner-Bielich J. Nucl Phys A, 2008, 804(1-4): 309
- [82] Haensel P, Zdunik J L, Bejger M, et al. A&A, 2009, 502(2): 605

*Note: Figure translations are in progress. See original paper for figures.*

*Source: ChinaXiv — Machine translation. Verify with original.*